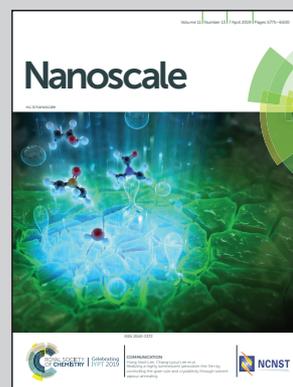**Showcasing research from the Department of Engineering Mechanics, Center for Flexible Electronics Technology, Tsinghua University, Beijing, China.**

Fabrication of highly pressure-sensitive, hydrophobic, and flexible 3D carbon nanofiber networks by electrospinning for human physiological signal monitoring

This work proposes a simple and cost-efficient strategy to fabricate versatile 3D carbon nanofiber networks (CNFNs) through electrospinning. The CNFNs with a high pressure-sensitivity demonstrate excellent mechanical and piezoresistive properties, which are capable of monitoring human physiological signals, such as phonation, pulse, respiration and human activities. An artificial electronic skin bioinspired by a human's hairy skin has been ingeniously proposed. In addition, the CNFNs possess other versatile characteristics, including ultralight weight, hydrophobicity, low thermal conductivity and low infrared emissivity, which opens up numerous opportunities for various applications.

ROYAL SOCIETY OF CHEMISTRY | Celebrating IYPT 2019

rsc.li/nanoscale

Nanoscale

Fabrication of highly pressure-sensitive, hydrophobic, and flexible 3D carbon nanofiber networks by electrospinning for human physiological signal monitoring†

Zhiyuan Han,[a,b] Zhiqiang Cheng, [ID] [c] Ying Chen,[d] Bo Li,[d] Ziwei Liang,[a,b] Hangfei Li,[a,b] Yinji Ma[a,b] and Xue Feng [ID] *[a,b]

Three-dimensional (3D) porous nanostructure materials have promising applications in pressure sensors or other situations. However, the low sensing sensitivity of these materials restricts precise detection of physiological signals, and it is still a challenge to manufacture highly pressure-sensitive materials, which simultaneously possess other versatile properties. Herein, a simple and cost-efficient strategy is proposed to fabricate versatile 3D carbon nanofiber networks (CNFNs) with superior pressure-sensitivity through electrospinning and thermal treatment. The pressure sensitivity of the CNFNs is 1.41 kPa^{-1}, which is much higher than that of similar 3D porous materials. Unlike traditional carbonaceous materials, the CNFNs exhibit excellent flexibility, stable resilience, and super compressibility (>95%), because of the nano-reinforce of Al_2O_3. Benefiting from the robust mechanical and piezoresistive properties of the CNFNs, a pressure sensor designed with the CNFNs is able to monitor human physiological signals, such as phonation, pulse, respiration and human activities. An arch-array platform for direction identification of tangential forces and an artificial electronic skin bioinspired by human's hairy skin have been ingeniously designed. The CNFNs also present other versatile characteristics as well, including ultralight density, hydrophobicity, low thermal conductivity, and low infrared emissivity. Therefore, the CNFNs have promising potential in a wide range of applications.

[a]*AML, Department of Engineering Mechanics, Tsinghua University, Beijing, 100084, China. E-mail: fengxue@tsinghua.edu.cn*
[b]*Center for Flexible Electronics Technology, Tsinghua University, Beijing, 100084, China*
[c]*College of Resources and Environment, Jilin Agriculture University, Changchun, 130118, China*
[d]*Institute of Flexible Electronics Technology of THU, Zhejiang, Jiaxing, 314000, China*

†Electronic supplementary information (ESI) available. See DOI: 10.1039/c8nr08341j

Introduction

Flexible, sensitive and low-cost pressure sensors have attracted scientific and commercial attention for various related applications, such as intelligent electronic skin,[1,2] personalized health monitoring,[3–5] and human–machine interaction.[6–8] Until now, sensing mechanisms of the emerged pressure sensors have been mainly based on piezoresistive,[9] piezoelectric,[10,11] pizeocapacitive,[12] and triboelectric effects,[13] and all the sensors demonstrate the sensitive ability to recognize mechanical stimuli. Notably, piezoresistive sensors, which can transduce pressure applied onto the sensors into a resistance signal, are widely used due to their remarkable advantages, including easy signal collection, being cost-efficient, and feasible preparation.[14] In resistive-type sensors, advanced materials assembled with micropatterned flexible substrates have been generally utilized to prepare highly sensitive pressure sensors.[9,15] For example, sensors with Au-deposited on polydimethylsiloxane (PDMS) micropillars,[16] a conductive elastomeric composite on a micropyramid array,[15] and Pt-coated interlocked nanofibers[9] all exhibit mechanical flexibility and high pressure-sensitivity. However, microstructures of these sensors are complicated to design and conductive materials are expensive, which limits their widespread applications. Therefore, a low-cost and simple fabrication of flexible piezoresistive materials still remains a huge challenge.

With the development of materials science, three-dimensional (3D) resilient nanostructures have been synthesized and utilized for pressure sensing, such as graphene–polyurethane sponge,[14] carbon black–polyurethane sponge,[6] carbon nanotube–polymer sponge,[17] carbon aerogels,[18] nanofiber-assembled cellular aerogels,[19] *etc.* 3D porous materials are generally attractive due to their high pressure-sensitivity, low density, large surface area, high porosity and other versatile
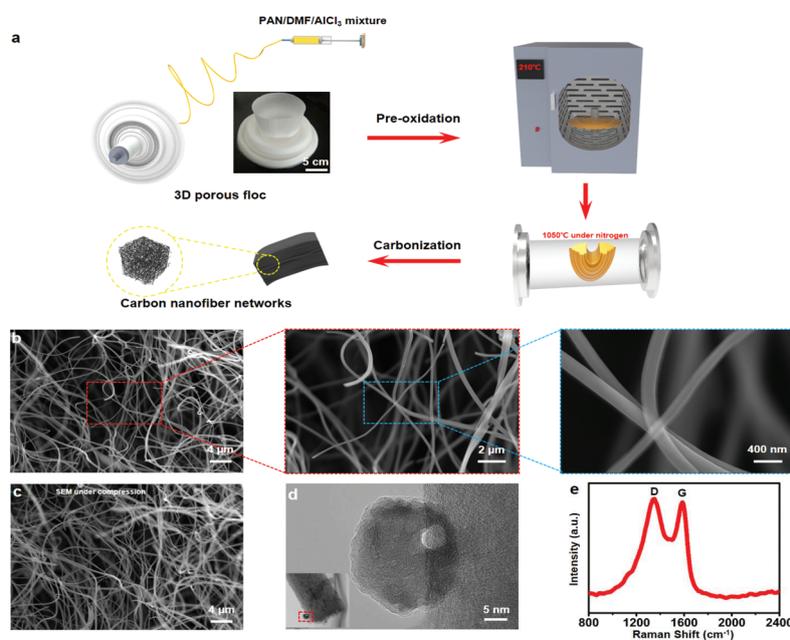
properties. They have been widely used for pressure sensing and other various applications. For instance, Qin and co-workers prepared a mechanically flexible graphene/polyimide nanocomposite foam for strain sensor applications, which exhibited a low density (10 mg cm^{-3}) and a high sensitivity (0.18 kPa^{-1}).[20] Another study reported a microcrack-designed carbon black@polyurethane sponge with a sensitivity of 0.023 kPa^{-1}.[6] Peng and co-workers proposed a hierarchical assembly strategy for fabricating nanocomposite foams with light weight, hydrophobicity, and superinsulating properties.[21] Despite these achievements, 3D materials have relatively low pressure-sensitivity and cannot simultaneously possess high sensitivity and versatile properties, which proposes a great challenge to fabricate multifunctional 3D materials with superior sensitivity.

In this work, versatile carbon nanofiber networks (CNFNs) with a superior sensitivity of 1.41 kPa^{-1} were fabricated using a cost-efficient and simple fabrication strategy. Through mature electrospinning and carbonization synthesis, 3D elastic bulk CNFNs rather than thin film networks[22–24] were directly prepared without freeze-drying.[25] During the preparation process, polyacrylonitrile (PAN) is a cheap industrial raw material and anhydrous aluminum chloride (AlCl$_3$) as a key addition contributes to the versatile characteristics. Meanwhile, the CNFNs overcome the brittle nature of conventional carbonaceous porous materials,[26,27] exhibiting robust mechanical properties, including fine flexibility, super compressibility (>95%), extraordinary resilience, and excellent fatigue resistance. To our knowledge, the sensitivity of our CNFNs is the highest in the 3D porous piezoresistive sponges and aerogels, which ensures their strong capability of monitor-

ing phonation, pulse, respiration, and movement of human joints. We have skillfully designed a platform for the direction identification of tangential forces and a bioinspired electronic skin by utilizing these outstanding properties. In addition, the CNFNs exhibit multifunctionality, such as low thermal conductivity, low infrared emissivity, hydrophobicity, and ultralight properties. Thus, they show promising potential for various applications.

Results and discussion

Fig. 1a illustrates the synthesis pathway of the CNFNs. Firstly, PAN and dimethylformamide (DMF) with certain concentrations were mixed by magnetic stirring. Followed by addition of AlCl$_3$, the precursor solution was prepared. Then the solution was loaded into a syringe. Under a certain experimental condition, 3D porous annular floc was directly prepared with the solution on a vegetable parchment-covered metallic rotating roller by electrospinning (see details in the Experimental section). Finally, the floc was pre-oxidized in an oven at 210 °C to obtain pre-oxidized nanofibers. The pre-oxidized nanofibers were carbonized into 3D porous CNFNs after thermal treatment at 1050 °C in a tube furnace under a nitrogen flow. As shown in the scanning electron microscopy (SEM) images (Fig. 1b), the CNFNs exhibited a porous, interconnected, 3D network structure, resulting in an ultralow density (3.6 mg cm^{-3}) and an ultrahigh porosity (~96%). The nanofibers with a diameter of 180–200 nm interweave with each other. PAN was chosen as the carbon source to make an electrospun precursor, since PAN-based materials are light weight with hydro-

Fig. 1 Synthesis and characterization of CNFNs. (a) Schematic illustration of the fabrication process of the CNFNs. (b) SEM images of CNFNs and the zoomed-in section with different magnifications. (c) SEM image of the same region with b (left) under compression, showing denser interwoven nanofibers. (d) TEM image of the CNFNs, which shows obvious lattice stripes of Al$_2$O$_3$. (e) Raman spectra pattern of the CNFNs.

phobicity.[28] In addition, PAN is an easily available and in-expensive raw material compared to other building units to achieve carbonaceous sponges, such as fullerenes, graphene, and carbon nanotubes.[29–31] During the fabrication process, $AlCl_3$ played the most important role in creating the 3D CNFNs with robust mechanical properties and thermal insulation.[24] Owing to the thermal treatment, the $AlCl_3$ was converted into Al_2O_3. The Al_2O_3 was homogeneously dispersed all over the fibers as shown in EDS mapping images (Fig. S3, ESI†). The dispersion strengthening effect was well formed by the Al_2O_3 reinforcements, which increased the fracture toughness of the CNFNs and improved the mechanical properties of the CNFNs. The CNFNs also exhibited excellent flexibility during bending and twisting (Fig. S1, ESI†). Furthermore, unlike traditional electrospinning into thin films, the 3D porous floc was directly prepared by electrospinning under a certain condition (see details in the Experimental section), and then the 3D nanofibrous CNFNs were readily fabricated through carbonization without freeze-drying. Therefore, this strategy with significant advantages of low cost and easy fabrication opens up a new method to produce 3D porous materials.

The elemental compositions of CNFNs were shown by a wide-scan X-ray photoelectron spectroscopy (XPS) profile, which were O, C and Al species (Fig. S2a, ESI†). The X-ray diffraction (XRD) pattern in Fig. S2b (ESI†) shows four characteristic peaks centered at 37.7°, 45.8°, 60.8°, and 66.8°, corresponding to the typical (311), (400), (511), and (440) planes of Al_2O_3, respectively. As shown in the transmission electron microscopy (TEM) image (Fig. 1d), an interlayer thickness of 0.25 nm in the small distorted lattice fringe belongs to the (400) plane of Al_2O_3. Meanwhile, the Al_2O_3 with good mechanical and chemical stability was evenly embedded all over the fibers, as presented in energy dispersive spectroscopy (EDS) images (Fig. S3, ESI†), which is attributed to the outstanding flexibility and elasticity of the CNFNs. Fig. 1e shows that the Raman spectrum of CNFNs displays two prominent peaks at around 1350 cm^{-1} and 1587 cm^{-1}, which correspond to the D-band and the G-band of graphitic carbon, respectively. The XRD pattern in Fig. S2b (ESI†) demonstrates that a broad peak at $2\theta = 24.8°$ further indicates a high graphitization degree.[32] Therefore, the CNFNs presented a desirable electrical conductivity (~9 S m^{-1}). When the tangled carbon nanofibers were compressed, the porous network became denser, the contact points between the fibers increased and the contact area of the fiber network increased a lot (see Fig. 1b (left) and Fig. 1c), which resulted in a decrease in the resistance of the CNFNs. In addition, the CNFNs can recover their original state when they are released from the compression, indicating that the CNFNs well exhibit the piezoresistive characteristics. The schematic pressure-sensing models are shown in Fig. S4.†

To demonstrate the high pressure-sensitivity, excellent resilience, and stable electrical properties of the CNFNs, a set of compressive tests and pressure-responsive experiments were performed (Fig. 2). Two types of samples are presented in Fig. 2a: one with source–drain electrodes on the same surface, while the other one with that on the opposite surfaces. To
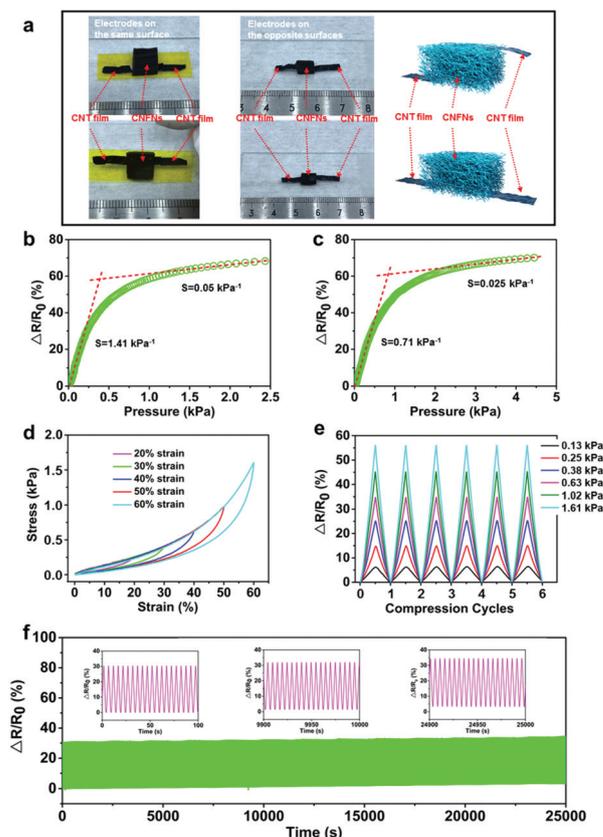

Fig. 2 Pressure-sensing and mechanical-electric characterization of the CNFNs. (a) Photographs of the testing structure of CNFNs with electrodes on the same side (left), with electrodes on the opposite sides (middle), and schematic illustrations (right). (b and c) Relative resistance change ratios as a function of the pressure for CNFNs with opposite-surface electrodes and coplanar electrodes, respectively. Both the two types exhibit high pressure-sensitivity. (d) Stress−strain curves of CNFNs with different set strains. (e) Multi-cycle compressive tests of variation in relative resistance with different applied pressures. (f) Cycling stability test of CNFNs under a repeated applied pressure of 0.38 kPa for 5000 cycles.

eliminate the contact resistance and obtain a stable signal output, carbon nanotube (CNT) films, used as lead electrodes, were conformally attached to the CNFNs with conductive silver paste due to the softness and thinness of the CNT films. Then the thin copper or silver wires were connected with the CNT film electrodes to increase the length for testing. Thus, the resistance variation was mainly caused by changes in the internal structure of the CNFNs. Fig. 2b and c show the electronic resistance variation ratios ($\Delta R/R_0 = (R_0 - R_P)/R_0$, where R_0 and R_P denote the resistance without and with applied pressure, respectively) versus the pressure of the CNFNs with opposite-surface electrodes and coplanar electrodes, respectively. Both types of samples exhibited higher pressure-sensitivity, compared to other similar research studies (Table S1, ESI†).[6,14,20,33,34] The sensitivity S can be defined as $S = \delta(\Delta R/R_0)/\delta P$, where P is the applied pressure. Fig. 2b and c display two obvious linear stages corresponding to differences
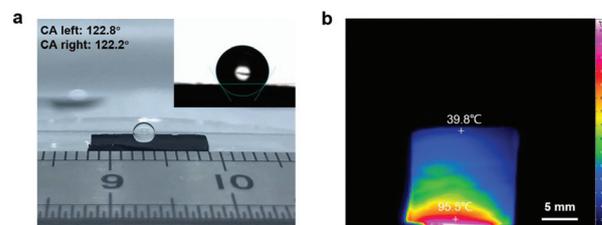
in sensitivity. For the sample with electrodes on the opposite surfaces (Fig. 2b), the calculated sensitivity is 1.41 kPa^{-1} in the range of 0–0.25 kPa, which is the highest in the previously reported 3D porous materials (Table S1, ESI†), while the sensitivity is 0.05 kPa^{-1} in the high-pressure range (1.25–2.5 kPa). For the sample with coplanar electrodes (Fig. 2c), the low-pressure segment in a range of 0–0.8 kPa exhibits a sensitivity of 0.71 kPa^{-1}, while it has a value of 0.025 kPa^{-1} in the high-pressure range (2.5–4.5 kPa). The differences in the lead mode of the electrodes can result in the different resistance changes of the CNFNs during compression. Two equivalent circuit models for these two designs are shown in Fig. S5† to explain the different resistance responses. In previous literature studies about 3D porous piezoresistive materials,[6,14,35] most of the lead modes were used by source–drain electrodes on the opposite sides, and they demonstrated strong ability in pressure sensing. Similarly, our sensor is capable enough of detecting human physiological signals because of its higher pressure-sensitivity (1.41 kPa^{-1}). However, the lead mode with coplanar electrodes can bring more advantages. It can reduce the probability of the breakage in the joint between electrodes and materials during cyclic working and contribute to broadening its applications, for example the following bio-inspired electronic skin. So all the sensors used the samples with electrodes on the same surface in the following experiments. Fig. S6 (ESI†) shows that the response time of the CNFN pressure sensor is less than 300 ms, which is fast enough to monitor human physiological signals. To investigate the detection limit of the sensors, a sliced silicon wafer (57 mg) was loaded and unloaded on a sensor with an area of 81 mm^2 (9 mm × 9 mm). The detection pressure is as low as 7 Pa (Fig. S7a, ESI†).

Compared with the brittle feature of the conventional carbonaceous networks, the CNFNs exhibited stable and robust mechanical characteristics. Fig. 2d plots a series of compressive stress–strain (σ–ε) curves of the CNFNs with different strains of 20, 30, 40, 50, and 60%. Two characteristic distinct regimes were obtained in the σ–ε curves: a linear elastic stage for ε < 30% with an elastic modulus of ~1.53 kPa and a densification stage for ε > 30% with a rising slope. The unloading curves can return to the initial loading point for different strains, which confirms that the CNFNs completely recover their original sizes without plastic deformations. The σ–ε curves of six compressive cycles at 50% strain were completely overlapped, as shown in Fig. S7b (ESI†). The CNFNs also display super compressibility, which can recover their original height even at an extreme strain of >95% (Movie S1, ESI†). To further demonstrate the stable and reliable resistance response, the multiple-cycle loading and unloading tests under various strains were carried out at the CNFN pressure. As shown in Fig. 2e, the resistance response of the CNFN pressure is synchronous with the variation of different applied pressures. Besides, the resistance variation ratios had a perfectly linear relationship with the corresponding strain, in which the Pearson's correlation coefficient is 0.9983 (Fig. S7c, ESI†). Fig. S7d (ESI†) describes that the relative resistance vari-

ation of the CNFN sensor is independent of the compression rates (0.05–0.25 Hz). The cycling stability of the CNFN sensor was investigated as well (Movie S2, ESI†). Fig. 2f shows that the resistance response of the sensor can be maintained during 5000 loading–unloading cycles (5 s for each cycle) under a pressure of 0.38 kPa, and no significant changes were found about the structure of the sample after the cycling test (Fig. S8, ESI†), which indicate a long working life, remarkable repeatability and stability of the CNFN sensor. All the results suggest that the CNFNs are suitable for preparing highly sensitive and stable pressure sensors to detect physiological signals.

Simultaneously, the CNFNs exhibited versatile properties, which had a great advantage over previous 3D porous materials (Table S1, ESI†). Due to their high porosity (96%), the CNFNs possessed high permeability when used as electronic skin and had an ultralow density of ~3.6 mg cm^{-3}. As shown in Fig. S9 (ESI†), the CNFNs were light enough to stably stand on the flower stamen and the dandelion, and a piece of CNFNs can float like a feather (Movie S3, ESI†). The inset in Fig. S9a (ESI†) shows that a CNFN sample with a volume of 1.7 cm^3 was weighed only 6.1 mg on the microbalance. This ultralight property allows the CNFNs to be used for detecting airflow and breathing. The specific surface area was as high as 238.18 m^2 g^{-1} measured by the BET method. Thus the CNFNs were an ideal material for the electrodes of lithium ion batteries and super capacitors, which are supposed to possess a high surface area and porosity.[36,37] Surface wettability of the CNFNs was tested by using a contact angle meter. Fig. 3a shows a water droplet on the surface of CNFNs with a contact angle of 122°, indicating its hydrophobicity. This hydrophobic property is caused by the additions of PAN[28] and Al$_2$O$_3$,[38] which can make the sensor designed by CNFNs waterproof and enable the application of CNFN sensors in humid environments. Aerogels generally are prominent thermal insulation materials with low conductivity, benefiting from their high porosity.[25] The thermal conductivity of the CNFNs was investigated by the transient plane source (TPS) method, and it (24 mW m^{-1} K^{-1}) is lower than that of most insulation materials.[25,39–41] The result indicates the prominent thermally insulating property of the CNFNs. As illustrated in Fig. 3b, temperature distribution dramatically decreased along the
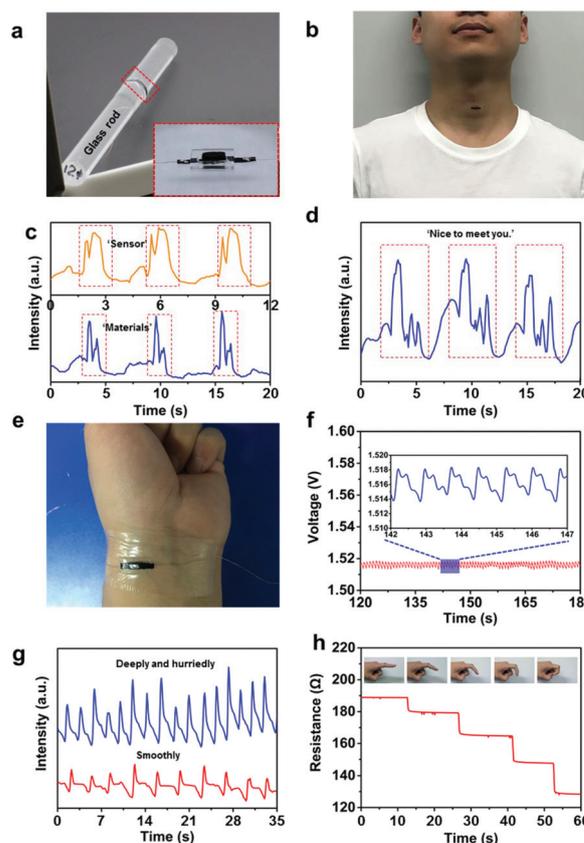

Fig. 3 Multifunctionality of the CNFNs. (a) Optical photograph of a water droplet on the surface of CNFNs. The inset shows the contact angle measurement of CNFNs, exhibiting high hydrophobicity with a contact angle of 122°. (b) Thermographic image of CNFNs on a 110 °C heating stage for 1 hour, indicating thermal insulation properties.

direction normal to the heat source (95.5 °C on the bottom and 39.8 °C on the top surface of the CNFNs). Therefore, the CNFNs have a good prospect as thermally superinsulating materials and the low thermal conductivity can make the artificial electronic skin designed by the CNFN sensor expand the property of thermal insulation. The infrared emissivity of the CNFNs was characterized by using an IR-dual-band infrared emissivity measuring instrument (Fig. S10, ESI†). It was as low as 0.62 compared to that of a similar research study,[42] which suggests a potential application for infrared stealth camouflage. The low infrared emissivity can also make the artificial electronic skin designed by CNFN sensors add the property of infrared stealth. These versatile properties could expand the applications of the artificial electronic skin designed by the CNFN sensor and indicate that the CNFNs are promising and effective as light weight thermal insulation or infrared stealth materials with hydrophobicity in a wide range of applications.

Owing to their high pressure-sensitivity and outstanding mechanical stability, the CNFN sensors show the superior capability of detecting human physiological signals, such as speech, pulse, respiration, and motion activities. To make the CNFN sensors more stable and reliable, polydimethylsiloxane (PDMS) supports and surgical semipermeable polyurethane films were applied to integrate with the pressure sensors (the inset in Fig. 4a and Fig. S11,† Experimental section). The shape of the PDMS support is a rectangular parallelepiped with a rectangular through hole, which just surrounds the CNFN sensor with coplanar electrodes. The PDMS supports not only guarantee a certain compression strain but also avoid the collapse of the sensor under a taut condition. The semipermeable film, which possesses excellent permeability of air and high quality of waterproofness, was used to attach the sensors onto the body. In addition, the semipermeable film further reduced the contact resistance between the CNFNs and CNT films by sticking them firmly. The sensor combined by the flexible components demonstrates excellent flexibility, which can be attached conformably onto a glass rod with a diameter of 12 mm (Fig. 4a). There was no obvious discomfort or inflammation when the sensor was pasted onto the volunteer's arm skin for 3 days, indicating the good biocompatibility of the sensor. Fig. 4b shows a CNFN sensor attached onto the neck to noninvasively monitor the muscle movement near throat during speech. The output signals of the sensor exhibit high resolution and distinct patterns for the pronunciation of the "sensor" and "materials", and the curves of each word have stable and repeatable characteristic peaks (Fig. 4c). Besides, the sensor can also identify phrases, such as "Nice to meet you.", as shown in Fig. 4d. Therefore, the CNFN sensor provides an effective and superior method for voice identification, which suggests a promising application in human–machine interactions. Wrist pulse is a significant medical index, which is closely related to the heart rate, blood pressure, and other assistant information for medical diagnosis. Fig. 4e shows a CNFN sensor fixed on the wrist to monitor the pulse in real time. The pulse waveform is clearly depicted in Fig. 4f, from which we can calculate that the heart rate was 75 beats

Fig. 4 Wearable device assembled from CNFNs for various physiological signal monitoring. (a) Photograph of the CNFN sensor twining around a glass rod with a diameter of 12 mm. The inset shows the structural composition of the sensor. (b) Optical image of the sensor attached to a human neck. (c and d) Real-time resistance response during pronouncing. (e) Photograph of the CNFN sensor fixed on the wrist to measure the pulse. (f) Pulse signal with clear waveforms, indicating 76 beats per min. (g) Respiratory signal caused by air movements for breathing smoothly and hurriedly, respectively. (h) Resistance responses of the CNFN sensor attached to the finger joint for different degrees of bending.

per minute and observe that every single pulse distinctly contained three characteristic peaks. The three peaks in a pulse waveform correspond to the percussion wave (P-wave), the tidal wave (T-wave) and the diastolic wave (D-wave), respectively (Fig. S12, ESI†). These results confirm that the CNFN sensor can accurately recognize detailed differences of the pulses, therefore indicating a potential application in medical diagnosis.
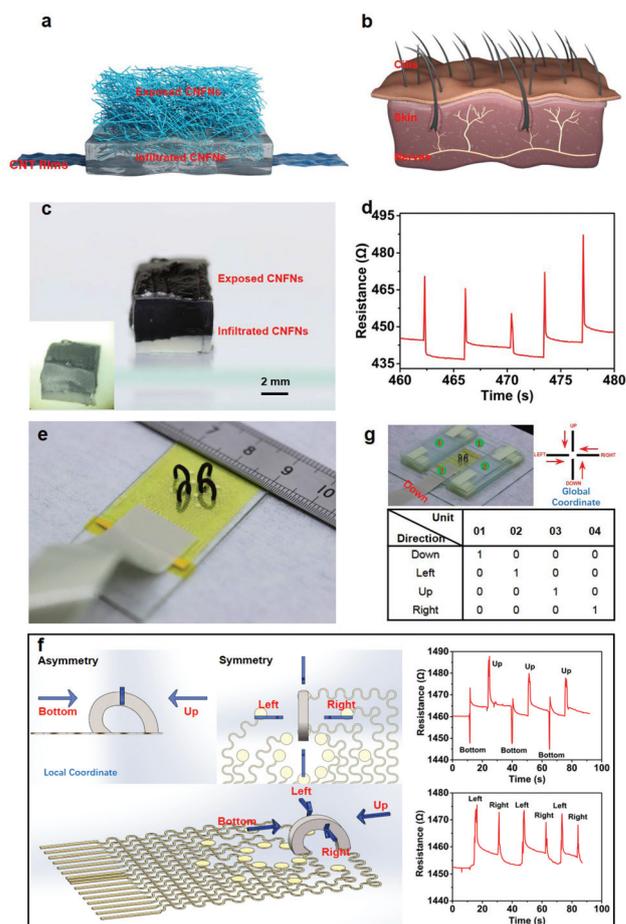
Moreover, the CNFN sensor demonstrates the utility for the respiration measurement, benefiting from the superlight property and the low detection limit of the CNFNs. A CNFN sensor was attached to the skin below the nostrils, similar to man's moustache. During breathing, the airflow from the nose disturbed the interweave situation of nanofibers, resulting in periodic changes of electrical resistance. As shown in Fig. 4g, the response of breathing in a relaxed and steady condition demonstrates a respiratory rate of 16 per minute, while the

respiratory frequency becomes denser (28 times per minute) and the average respiratory intensity for hurried and deep breathing is higher than that of breathing in a relaxed condition. The stable and reliable response to breath suggests a possible application to monitor diseases related to respiration, such as respiratory distress syndrome. Apart from tiny deformation detection, our CNFN sensor can also recognize large deformation caused by human activities due to its super compressibility. The motion of finger joints was relatively large, so we pasted a sensor onto the joint of the index finger as a representative case. Fig. 4h shows that the resistance variation increases with the deformation of the finger's joint. Fig. S13 (ESI†) shows that the CNFN sensor fixed on the knee joint displays repeatable and stable resistance variation response during bending and straightening.

Bio-inspired by human's hairy skin, an artificial electronic skin was designed using the CNFN sensor with coplanar electrodes. Fig. 5a shows that the e-skin mainly consists of three parts: CNT film electrodes, exposed CNFNs, and bottom CNFNs infiltrated with an elastic matrix (Ecoflex, Smooth-On Inc.). It is worth noting that the viscosity of Ecoflex should not be too thick or too thin. Ecoflex cannot infiltrate into the CNFNs when it is too thick, while it can filter totally into the whole CNFNs due to capillarity when it is too thin. Therefore, we chose the Ecoflex 00-30. The interface between the exposed CNFNs and the infiltration section is clearly shown in Fig. 5c. The e-skin is functionally similar to the structure of human's ciliated skin (Fig. 5b), which is sensitive to tiny pressure and even air vibration, in which, the outmost CNFNs of the e-skin are equivalent to the fine hair on human skin as a tactile receptor, and the hydrophobicity of the CNFNs contributes to the waterproof protection of the e-skin. The Ecoflex-infiltrating section corresponds to the skin, increasing mechanical flexibility and stretchability. The CNT film electrodes are responsible for transmitting electrical signals, which is an analogy of nerve bundles in skin to communicate with the brain. As illustrated in Fig. 5d, the e-skin can respond sensitively to airflow caused by using a rubber suction bulb. It has promising potential for fabricating a waterproof, thermal insulating, infrared stealth, ultrahigh pressure-sensitive artificial e-skin.

Apart from normal pressure detection, an arch-array sensor platform (Fig. 5e) was designed to distinguish the direction of tangential forces. Firstly, four CNFN components were cut into a shape of a square prism (a cross-section area of 1 mm × 1 mm, a height of 8 mm) due to the super compressibility and excellent elasticity. Both ends of every prism were pasted steadily on the corresponding electrodes (Fig. S14, ESI†) by silver paste. The electrodes were fabricated by conventional lithography and etching.[43] We first pasted one end of the prism onto the inner side of the electrodes ('−'), and then fixed the other end to the outer side ('+'), thus intentionally resulting in a slightly asymmetric structure of the CNFN prism in the bottom-up direction and a symmetric structure in the left-right direction in the local coordinate of every prism unit (Fig. 5f). Due to the symmetry in the left-right direction (the upper right corner in the left section of Fig. 5f), when the tangential force

Fig. 5 Bioinspired artificial electronic skin and platform for the direction discrimination of tangential forces with CNFNs. (a and b) Schematic illustration of the bioinspired artificial e-skin, by analogy with the structure of human's hairy skin. (c) Optical photograph of the interface between the exposed CNFNs and the infiltrated section for the e-skin. (d) Resistance response of the artificial e-skin to airflow by a rubber suction bulb. (e) Photograph of the anch-arry sensor platform for recognizing directions of tangential forces. (f) The schematic diagrams of the arch CNFN unit, showing the asymmetry in the bottom-up direction and the symmetry in the left-right direction in the local coordinate of every prism unit, and the resistance response of the arch CNFN unit for tangential forces with different directions. (g) Photograph of the special loading device and the response results of the platform to tangential forces with four different directions.

from the left to right direction and from the right to left direction was applied at the top of the prism, the internal deformation of the whole prism was almost the same. The resistance response to the tangential force was the same. Because of the asymmetry of the CNFN prism in the bottom-up direction, the internal deformation of the whole prism was different when the tangential force from the bottom to top direction and from the up to down direction was applied at the top of the prism. The resistance response to the tangential force from the bottom to top direction and from the up to down direction was different. In addition, we experimentally observed that the asymmetry of the prism caused contrary

resistance response under tangential forces with different directions. To ensure that the resistance variation was induced just by a tangential force rather than normal pressure, a home-made loading device was designed by using a glass slide (Fig. 5g, and Movie S4, ESI†), which only allowed the loading slide move in the horizontal direction. The resistance of the CNFN prism increased when loading the slide from up to bottom, while the resistance decreased upon sliding from bottom to up because of the asymmetry of the CNFN prism in the bottom-up direction (Fig. 5f, and Movie S4, ESI†). Due to the bilateral symmetry of the CNFN prism in the left-right direction, the resistance both increased whether loading from the left to right or from right to left direction among which we define the direction of the inner side ('−') as a direction of 'bottom' in the local coordinate of every prism (Fig. S14, ESI†). Benefiting from this characteristic of the CNFN prism, an array platform with four similar units was fabricated to discriminate directions of tangential forces, and the response of the platform is shown in Fig. 5g under loading with different directions. It is worth noting that we defined 'down' in the global coordinate of the arch-array platform to differ from 'bottom' in the local coordinate of every prism, and we marked the increase in resistance as '0' and the decrease in resistance as '1'. For example, the result number '1000' of the four units means that the direction of the loading tangential force is 'down' in the global coordinate of the arch-array platform, and the result number '0100' of the four units means that the direction of the loading tangential force is 'left' in the global coordinate of the arch-array platform. Therefore, the direction of tangential forces can be identified by the encoding of the four-array platform. This array platform provided an efficient and potential strategy for detecting the directions of tangential forces or even the magnitude of the forces.

Conclusions

In summary, a versatile 3D CNFN with an ultrahigh pressure-sensitivity was synthesized through an economic electrospinning and thermal carbonization strategy. This strategy breaks the limitations of electrospinning into thin films and surmounts the fragile nature of carbon-based materials, leading to 3D porous carbon nanofiber networks with excellent resilience. The pressure sensitivity of 1.41 kPa^{-1} is higher than that of previous 3D porous materials, and the outstanding repeatability (5000 times), fast response time (<300 ms), and super compressibility (>95%) of the CNFNs all contribute to pressure sensing. Meanwhile, the CNFNs exhibited comprehensive versatility, including mechanical flexibility, an ultralight density of 3.6 mg cm^{-3}, hydrophobicity, a relatively low thermal conductivity (23 mW m^{-1} K^{-1}), and a low infrared emissivity (0.62). Benefiting from the high sensitivity and robust mechanical properties of CNFNs, a CNFN pressure sensor was prepared to detect both subtle and large deformation. It has demonstrated promising potential for monitoring human physiological signals, such as phonation, pulse, respiration and joints' movement. The arch-array platform and e-skin provide new ideas for subsequent research studies. In addition, the multifunctionality of the CNFNs opens up numerous opportunities for various applications in, for example, antifrosting coating, electrodes of lithium ion batteries or supercapacitors, thermal insulation, and infrared stealth.

Experimental section

Preparation of CNFNs

The solution was prepared by adding 1.2 g of polyacrylonitrile (PAN) to 8.8 g of dimethylformamide (DMF) with magnetic stirring at 60 °C for 6 h. Then, 0.3 g of AlCl$_3$ was added, followed by magnetic stirring at room temperature for 5 h to obtain the precursor solution. The precursor solution was loaded into a syringe, which was connected with a high voltage of 15 kV. The feed rate of the solution was controlled at 0.6 mL h^{-1}, and the distance between the needle and the rotate acceptor was 20 cm. The humidity of the electrospinning condition was below 40% and the temperature was at room temperature. Under these specific conditions, the 3D fibrous annular floc was directly prepared on a vegetable parchment-covered metallic rotating roller. Then, the 3D floc was pre-oxidized at 210 °C for 60 minutes to obtain pre-oxidized nanofibers. Finally, the pre-oxidized nanofibers were carbonized in a tube furnace at 1050 °C under a nitrogen atmosphere, and the temperature was raised at 5 °C min^{-1}, held at 1050 °C for 60 minutes and naturally cooled to obtain the 3D porous CNFNs.

Fabrication of PDMS supports

The PDMS (184, SLGARD, USA) elastomer consisting of a prepolymer and a cross-linker was mixed in ratios of 10:1 (measured by weight). Then the mixture was placed in a vacuum chamber up to 20 min for degassing. The vacuum degassed PDMS was poured into a plastic culture dish to a height of two-thirds that of the CNFN sensor. After the PDMS was cured at a constant temperature of 65 °C for 240 min, we cut out a rectangular parallelepiped with a rectangular through hole, where the size of the hole was just larger than that of the CNFN sensor so that the sensor could be surrounded by the PDMS supports. The bottoms of the PDMS support and the sensor were both attached to the semipermeable polyurethane film (1624 W, Tefaderm film, 3 M), to form the whole structure (see the inset in Fig. 4a).

Characterization details

The micromorphology and microstructure of the samples were observed using a SEM (GeminiSEM 500) and a TEM (JEM-2100F). The XRD pattern was measured on a Bruker D8 diffractometer. Raman spectra were recorded using a laser with a wavelength of 532 nm (LabRAM HR Evolution). XPS spectra were recorded on a Thermo Scientific ESCALAB 250Xi (with an exciting source of Al Kα (1286.6 eV)). The contact angle was measured with a contact angle meter (OCA20,

Dataphysics). The surface area was measured by the BET method (Autosorb-iQ2-MP). The porosity was calculated by the water saturation method. Thermal conductivity and infrared emissivity were measured by using a conductivity meter (TPS 2500S, Hot Disk) and an emissivity meter (TSS-5X, Japan Sensor Corporation), respectively. Compression tests were carried out with a testing machine (Zwick-Z005) and a fatigue machine (Instron-8874, USA), while the electrical signals were recorded through a resistance instrument (TH2515, China) and a voltage acquisition card (NI USB-4431), where a resistance instrument was for most resistance tests and DAQ was for high-resolution acquisition.

Conflicts of interest

There are no conflicts to declare.

Acknowledgements

References

1 J. Kang, D. Son, G.-J. N. Wang, Y. Liu, J. Lopez, Y. Kim, J. Y. Oh, T. Katsumata, J. Mun, Y. Lee, L. Jin, J. B.-H. Tok and Z. Bao, *Adv. Mater.*, 2018, **30**, 1706846.

2 J. Kim, M. Lee, H. J. Shim, R. Ghaffari, H. R. Cho, D. Son, Y. H. Jung, M. Soh, C. Choi, S. Jung, K. Chu, D. Jeon, S.-T. Lee, J. H. Kim, S. H. Choi, T. Hyeon and D.-H. Kim, *Nat. Commun.*, 2014, **5**, 5747.

3 T. Wang, H. Yang, D. Qi, Z. Liu, P. Cai, H. Zhang and X. Chen, *Small*, 2018, **14**, 1702933.

4 L. Y. Chen, B. C.-K. Tee, A. L. Chortos, G. Schwartz, V. Tse, D. J. Lipomi, H.-S. P. Wong, M. V. McConnell and Z. Bao, *Nat. Commun.*, 2014, **5**, 5028.

5 C. Choi, M. K. Choi, T. Hyeon and D.-H. Kim, *ChemNanoMat*, 2016, **2**, 1006–1017.

6 X. Wu, Y. Han, X. Zhang, Z. Zhou and C. Lu, *Adv. Funct. Mater.*, 2016, **26**, 6246–6256.

7 B. Xu, A. Akhtar, Y. Liu, H. Chen, W. H. Yeo, S. I. Park, B. Boyce, H. Kim, J. Yu, H. Y. Lai, S. Jung, Y. Zhou, J. Kim, S. Cho, Y. Huang, T. Bretl and J. A. Rogers, *Adv. Mater.*, 2016, **28**, 4462–4471.

8 H.-J. Kim, A. Thukral and C. Yu, *ACS Appl. Mater. Interfaces*, 2018, **10**, 5000–5006.

9 C. Pang, G.-Y. Lee, T.-i. Kim, S. M. Kim, H. N. Kim, S.-H. Ahn and K.-Y. Suh, *Nat. Mater.*, 2012, **11**, 795.

10 B. Lu, Y. Chen, D. Ou, H. Chen, L. Diao, W. Zhang, J. Zheng, W. Ma, L. Sun and X. Feng, *Sci. Rep.*, 2015, **5**, 16065.

11 C. Dagdeviren, B. D. Yang, Y. Su, P. L. Tran, P. Joe, E. Anderson, J. Xia, V. Doraiswamy, B. Dehdashti, X. Feng, B. Lu, R. Poston, Z. Khalpey, R. Ghaffari, Y. Huang, M. J. Slepian and J. A. Rogers, *Proc. Natl. Acad. Sci. U. S. A.*, 2014, **111**, 1927–1932.

12 S. Y. Kim, S. Park, H. W. Park, D. H. Park, Y. Jeong and D. H. Kim, *Adv. Mater.*, 2015, **27**, 4178–4185.

13 Z. W. Yang, Y. Pang, L. Zhang, C. Lu, J. Chen, T. Zhou, C. Zhang and Z. L. Wang, *ACS Nano*, 2016, **10**, 10912–10920.

14 H. B. Yao, J. Ge, C. F. Wang, X. Wang, W. Hu, Z. J. Zheng, Y. Ni and S. H. Yu, *Adv. Mater.*, 2013, **25**, 6692–6698.

15 C.-L. Choong, M.-B. Shim, B.-S. Lee, S. Jeon, D.-S. Ko, T.-H. Kang, J. Bae, S. H. Lee, K.-E. Byun, J. Im, Y. J. Jeong, C. E. Park, J.-J. Park and U.-I. Chung, *Adv. Mater.*, 2014, **26**, 3451–3458.

16 H. Park, Y. R. Jeong, J. Yun, S. Y. Hong, S. Jin, S.-J. Lee, G. Zi and J. S. Ha, *ACS Nano*, 2015, **9**, 9974–9985.

17 J.-W. Han, B. Kim, J. Li and M. Meyyappan, *Appl. Phys. Lett.*, 2013, **102**, 051903.

18 H. Zhuo, Y. Hu, X. Tong, Z. Chen, L. Zhong, H. Lai, L. Liu, S. Jing, Q. Liu, C. Liu, X. Peng and R. Sun, *Adv. Mater.*, 2018, **30**, 1706705.

19 S. Zhou, T. You, X. Zhang and F. Xu, *ACS Appl. Nano Mater.*, 2018, **1**, 2095–2103.

20 Y. Qin, Q. Peng, Y. Ding, Z. Lin, C. Wang, Y. Li, F. Xu, J. Li, Y. Yuan, X. He and Y. Li, *ACS Nano*, 2015, **9**, 8933–8941.

21 Q. Peng, Y. Qin, X. Zhao, X. Sun, Q. Chen, F. Xu, Z. Lin, Y. Yuan, Y. Li, J. Li, W. Yin, C. Gao, F. Zhang, X. He and Y. Li, *ACS Appl. Mater. Interfaces*, 2017, **9**, 44010–44017.

22 A. Greiner and J. H. Wendorff, *Angew. Chem., Int. Ed.*, 2007, **46**, 5670–5703.

23 M. Wang, Z.-H. Huang, L. Wang, M.-X. Wang, F. Kang and H. Hou, *New J. Chem.*, 2010, **34**, 1843–1845.

24 O. Y. Kweon, S. J. Lee and J. H. Oh, *NPG Asia Mater.*, 2018, **10**, 540–551.

25 Y. Si, J. Yu, X. Tang, J. Ge and B. Ding, *Nat. Commun.*, 2014, **5**, 5802.

26 W.-E. Teo, R. Inai and S. Ramakrishna, *Sci. Technol. Adv. Mater.*, 2011, **12**, 013002.

27 L. Jin, Z.-Q. Feng, T. Wang, Z. Ren, S. Ma, J. Wu and D. Sun, *J. Mater. Chem. B*, 2014, **2**, 129–136.

28 F. Hochart, R. De Jaeger and J. Levalois-Grützmacher, *Surf. Coat. Technol.*, 2003, **165**, 201–210.

29 A. Roh, H. Y. Um, D. Kim, S. Nam, H. S. Kim and H. Choi, *J. Mater. Sci.*, 2017, **52**, 11988–12000.

30 L. Qiu, J. Z. Liu, S. L. Y. Chang, Y. Wu and D. Li, *Nat. Commun.*, 2012, **3**, 1241.

31 H. Sun, Z. Xu and C. Gao, *Adv. Mater.*, 2013, **25**, 2554–2560.

32 M. Biswal, A. Banerjee, M. Deo and S. Ogale, *Energy Environ. Sci.*, 2013, **6**, 1249–1259.

33 Y. Si, X. Wang, C. Yan, L. Yang, J. Yu and B. Ding, *Adv. Mater.*, 2016, **28**, 9512–9518.

34 C. Mu, Y. Song, W. Huang, A. Ran, R. Sun, W. Xie and H. Zhang, *Adv. Funct. Mater.*, 2018, **28**, 1707503.

35 Y. Guo, Z. Guo, M. Zhong, P. Wan, W. Zhang and L. Zhang, *Small*, 2018, **14**, 1803018.

36 Z.-Y. Wu, H.-W. Liang, B.-C. Hu and S.-H. Yu, *Angew. Chem., Int. Ed.*, 2018, **130**, 15872–15889.

37 Z. Niu, W. Zhou, X. Chen, J. Chen and S. Xie, *Adv. Mater.*, 2015, **27**, 6002–6008.

38 H. Fang, J. Gao, H. Wang and C. Chen, *J. Membr. Sci.*, 2012, **403**, 41–46.

39 N. Leventis, C. Chidambareswarapattar, D. P. Mohite, Z. J. Larimore, H. Lu and C. Sotiriou-Leventis, *J. Mater. Chem.*, 2011, **21**, 11981–11986.

40 M. D. Gawryla, M. Nezamzadeh and D. A. Schiraldi, *Green Chem.*, 2008, **10**, 1078–1081.

41 H. Wang, X. Zhang, N. Wang, Y. Li, X. Feng, Y. Huang, C. Zhao, Z. Liu, M. Fang, G. Ou, H. Gao, X. Li and H. Wu, *Sci. Adv.*, 2017, **3**, e1603170.

42 S. Fang, W. Wang, X. Yu, H. Xu, Y. Zhong, X. Sui, L. Zhang and Z. Mao, *Mater. Lett.*, 2015, **143**, 120–123.

43 Y. Chen, B. Lu, Y. Chen and X. Feng, *Sci. Rep.*, 2015, **5**, 11505.